Journal of Nanobiotechnology

RESEARCH Open Access

PDGFR-α shRNA-polyplex for uveal melanoma treatment via EMT mediated vasculogenic mimicry interfering

Jiahao Wang[1], Zhirong Chen[1], Peiyi Zhao[1], Yajia Wang[1], Jiang Chen[1] and Quankui Lin[1*]

Abstract

Up to 50% of individuals with uveal melanoma (UM), a frequent cancer of the eye, pass away from metastases. One of the major challenges in treating UM is the role of receptor tyrosine kinases (RTKs), which mediate the epithelial-mesenchymal transition (EMT) of tumors. RTKs are involved in binding multiple growth factors, leading to angiogenesis and vasculogenic mimicry (VM) phenomena. Currently, most anti-angiogenic drugs have shown a tendency to increase the VM of tumors in clinical trials, resulting in limited efficacy. The existing gap in UM treatment lies in the lack of effective strategies to target RTK-mediated EMT and VM. While some approaches have been attempted, there is still a need for novel therapeutic interventions that can specifically interfere with these processes. This research employed the gene vector PEI-g-PEG to interfere with the platelet derived growth factor-alpha receptor (PDGFR-α)-mediated EMT process, thereby retarding the growth of UM. The cell experiments demonstrated that the gene polyplex exhibited favorable cell uptake and lysosome escape properties, effectively suppressing the expression of PDGFR-α protein and EMT marker proteins and the occurrence of VM phenomenon. In vivo animal studies also inhibited the growth of UM, and PAS assays showed that the treatment reduced the generation of VM in tumor tissue. This study broadens the application of PEI-g-PEG while interfering with the RTK-mediated tumor EMT process with the help of RNAi technology, providing a new idea for tumor reduction research.

Keywords PEI-g-PEG polyplex, RNA interfering, Uveal melanoma, Angiogenesis, Vasculogenic mimicry

Introduction

Uveal melanoma (UM) is the most common intraocular malignancy in adults arising from melanocytes of the choroid, ciliary body, and iris [1–3]. Although treatment strategies such as patch irradiation, local resection, and enucleation provide a local curative effect, up to 50% of UM patients still die from distant tumor metastasis, making it impossible to eliminate completely by surgery [4, 5]. The leakage of growth factors caused by the tumor itself or by the effects of radiotherapy allows the production of neovascularization within the UM tumor as well as vasculogenic mimicry (VM) [6, 7]. All the above reasons lead to tumor recurrence, metastasis and drug resistance.

Many aspects are involved in tumor growth, invasion and metastasis. Epithelial-mesenchymal transition (EMT) refers to the transformation of cells from an epithelial phenotype to a mesenchymal phenotype [8–11]. This process determines embryonic development and cancer progression, assisting tumor plasticity [12].

*Correspondence:
Quankui Lin
linqk@wmu.edu.cn
[1]National Engineering Research Center of Ophthalmology and Optometry, School of Biomedical Engineering, School of Ophthalmology and Optometry, Eye Hospital, Wenzhou Medical University, Wenzhou 325027, China

Through the process of EMT, tumor cells can acquire the ability to disarm anti-tumor defenses in vivo, resist apoptosis and anti-tumor drugs, spread in the body, and expand the number of tumor cells [13]. Likewise, VM is an extravascular mechanism in aggressive tumors directing circulation [14–16]. It is a vessel-like channel that follows the deformation of the cells themselves, increased migration capacity, and remodeling of the extracellular matrix, unlike classical angiogenesis [17, 18]. These resulting microvessels and vascular channels are major components of the tumor microvasculature that supports tumor growth and metastasis.

Targeting angiogenesis appears to be an attractive and reasonable strategy for the treatment of uveal melanoma [19, 20]. However, most anti-angiogenic drugs were ineffective in clinical trials [21, 22], and bevacizumab may increase angiogenic mimicry in uveal melanoma [23, 24]. This phenomenon has also been the reason for the failure of anti-angiogenic therapy in other cancers [25, 26]. Related studies have also confirmed that the regulatory factors and transcription factors related to EMT in VM are significantly increased [27], indicating that EMT plays a key role in the formation of VM [25]. Therefore, investigation of the molecular and cellular basis of EMT for tumor therapy should start with two vascular mechanisms that may lead to new long-term therapeutic strategies [28].

PDGFR-α is required for the development of the lung, intestinal villi and facial bones, as well as for hair follicle morphogenesis, spermatogenesis, oligodendrocyte and astroglial cell development [29]. On the other hand, oncogenic mutations of PDGFR and overexpression of PDGF/PDGFR members are associated with the cancer tumor microenvironment [30]. The binding of platelet-based growth factor (PDGF) to its receptor PDGFR-α activates cellular signaling pathways [31–33], including phosphatidylinositol 3-kinase and extracellular signal-regulated kinasepathway [34], whose activation occurs in endothelial cells to promote cell proliferation, survival and migration, thereby promoting angiogenesis. At the same time, PDGFR-α is related to the EMT of various cancers and participates in the formation of tumor cell VM.

Gene therapy has shown great promise in basic and clinical biomedical research, particularly in cancer treatment. Among them, RNA interference (RNAi) technology is considered a possible cancer treatment strategy [35, 36]. Because siRNAs attack and destroy the corresponding mRNA, they have emerged as promising tools for silencing the expression of oncogenes in various cancers by simply changing the siRNA sequence [37, 38]. However, the search for safe and effective delivery vehicles for nucleic acids has always been a major challenge for gene therapy [39, 40]. Viral vectors such as adenoviruses and retroviruses were originally used for efficient expression in various cell lines [41, 42]. However, problems such as inherent immunogenicity or insertional mutations become major limitations in clinical application [43, 44]. Nonviral vectors have attracted great interest due to their advantages in overcoming many limitations of viral vectors, especially their high loading capacity and excellent biocompatibility [45]. Many nanostructured nonviral vectors have been studied, including organic vehicles (liposomes, polymers, peptides, etc.) and inorganic vehicles (silica, carbon tubes, etc.) [46]. The transfection properties of polyethyleneimine-grafted-polyethylene glycol (PEI-g-PEG) as a nonviral vector have been demonstrated in previous studies [47].

In this study, the PEI-g-PEG /PDGFR-α shRNA nanoparticle was prepared using an electrostatic conjugation approach following the gene encapsulation properties of PEI-g-PEG, which inhibited the tendency of VM formation in tumor cells by interfering with the EMT process, while limiting tumor growth by controlling angiogenesis through PDGF-RTK cascade signaling. The results suggest that this approach could be a promising new idea for controlling the development of uveal melanoma (Scheme 1).

Materials and methods

Reagents and antibodies

Polyethyleneimine with a molecular weight of 25,000 Da (PEI), and fluorescein isothiocyanate (FITC) were purchased from Sigma-Aldrich. PEI-g-PEG (PEI Mn=25000, PEG segment Mn=2000) were provided by Ruixi Bio. Dulbecco's modified Eagle's medium (DMEM), Fetal bovine serum (FBS), 0.05% trypsin-EDTA, penicillin-streptomycin solution and other cell culture-related reagents were purchased from Gibco. Phosphate-buffered saline (PBS) was purchased from Boster Biological Technology. Matrigel 356,234 and 356,230 were purchased from Corning®.

The cell counting kit-8(CCK-8), Hoechst 33,342, 4% paraformaldehyde fix solution, Periodic Acid-Schiff Staining Kit (PAS), Lyso-Tracker Red(lysosome red fluorescent probe, LT-Red), 1,1'-dioctadecyl-3,3,3',3'-tetramethylindocarbocyanine (DiI), DAPI Staining Solution, Antifade Mounting Medium with DAPI, enhanced BCA protein assay (BCA) kit, BeyoClick™ EdU Cell Proliferation Kit with Alexa Fluor 488, Nucleic acid electrophoresis and recovery package, Plasmid Maxi Preparation Kit for All Purpose and RIPA lysis buffer were provided by Beyotime Biotechnology Co. Fish sperm DNA was purchased from Aladdin.

Antibodies against PDGFR-α and E-cadherin were purchased from Santa Cruz and Immunoway. All other secondary antibodies were from Santa Cruz.

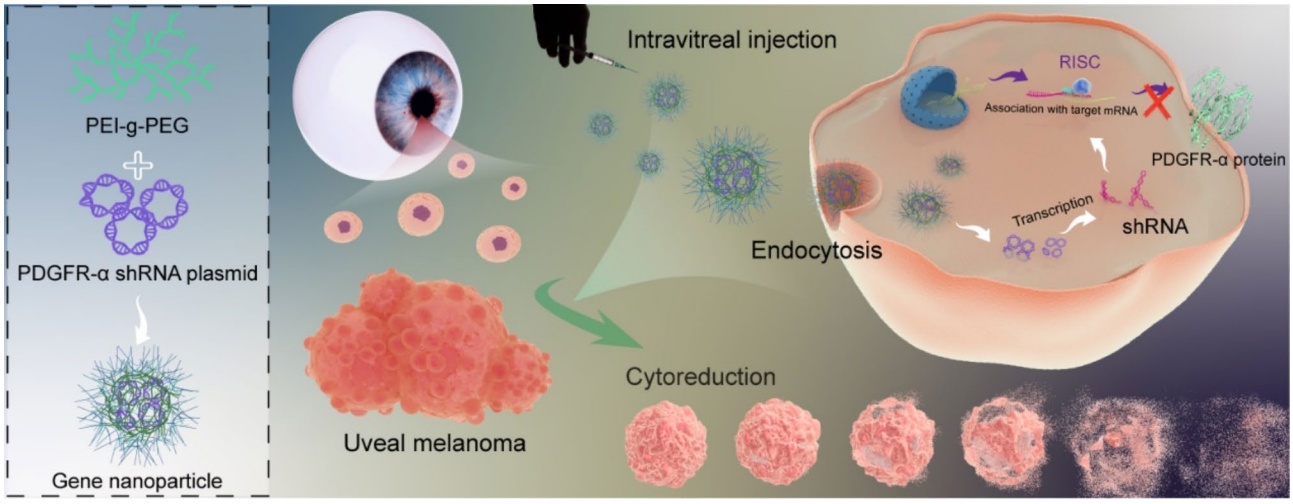

Scheme 1 Schematic illustration of gene nanoparticles PEI-g-PEG/PDGFR-α shRNA interfere with the EMT process to inhibit vasculogenic mimicry for the reduction of uveal melanoma

Preparation of the gene polyplex

Introduction of the plasmid

The reporter plasmid DNA, encoding an enhanced green fluorescent protein (GFP-pCAGGS), was amplified in the lab from a recombinant plasmid containing Escherichia coli clones, which were kindly provided by Prof. JG Chen (Wenzhou Medical University), and purified using the Plasmid Maxi Preparation Kit for all experiments. The PDGFR-α shRNA plasmid DNA (PTSB-SH-mCherry-2 A-NEO) was also propagated in Escherichia coli DH5α (Tsingke Biotechnology Co., Ltd., China). Its four coding sequences are as follows.

shRNA1	**CCGGGATGATCTGCAAGCATATTAACTC-GAGTTAATAYGCTTGCAGATCATCTTTTTT**
shRNA2	CCGGGCCAGCAATCTCTCAAATATTCTCGAG AATATTTGAGACATTGCTGGCTTTTTT
shRNA3	CCGGCGTTCAAGACCAGCGAGTTTACTCGA GTAAACTCGCTGGTCTTGAACGTTTTTT
shRNA4	CCGGAGTGGCCATTACACCATTATACTCGAG TATAATGGTGTAATGCCACTTTTTTT

The concentration of DNA was determined by measuring the UV absorbance at 260 and 280 nm with the Ultraviolet-visible spectrophotometer (DS-11, Denovix, America), and the purified DNA was stored at -20 ℃.

Synthesis of PPD, PPG, and PPshn

PEI-g-PEG/DNA (PPD) polyplex were obtained by electrostatic association. Briefly, PEI-g-PEG and the fish sperm DNA were dissolved in DEPC water (DNase/RNase free) at different N/P ratios (molar ratio of amino groups of PEI-g-PEG to phosphorus element of DNA). The reacted mixture was vortexed for 30 s and allowed to stand at 25 °C for 30 min. PPD is used for characterization and in vitro biocompatibility experiments. Gene nanoparticles loaded with different plasmid DNA encoding reporter genes were formed separately. They were named PEI-g-PEG/GFP (PPG), and PEI-g-PEG/PDGFR-α shRNAn (PPShn, n stands for 1,2,3,4).

Characterization of the gene polyplex

The particle size and zeta potential of the particles (the final concentration of DNA was 0.3 mg/mL) were determined by dynamic light scattering (DLS, Malvern Instrument Ltd, Malvern, UK) at room temperature [48]. The ability of polymers to bind with DNA was measured by gel electrophoresis with different N/P ratios (0, 5, 7, 10, 15, and 20) [49]. The morphological characteristic of PPD (N/*P*=10) was observed by transmission electron microscope (TEM, FEI Talos F200, America). To test the storage stability of the gene polyplex, the prepared PPD (N/*P*=10) solution was stored statically in a refrigerator at 4 °C, and its particle size potential was continuously detected for 7 days.

Cell culture

The human uveal melanoma cell lines OCM-1 and the human umbilical vein endothelial cells (HUVECs). HUVECs were used for the experiment on tube formation [50–52]. The two cell lines were incubated in RPMI-1640 and DMEM complete medium, respectively. The human embryonic kidney cell lines (HEK 293T) used DMEM complete medium. The complete medium also contained 10% FBS and 1% penicillin-streptomycin solution. All cells were cultured at 37 ℃ in a humidified incubator containing 5% CO_2.

In vitro cytotoxicity of the gene polyplex

The in vitro cytotoxicity of PPD was studied by the CCK-8 assay [53, 54]. Briefly, cells were grown with 100

μL complete medium at a density of 5000 cells/well in 96-well plates for 24 h. Subsequently, the PPD solutions with different N/P ratios (5, 10, 20, 40) were added. Untreated cells were used as controls. After 48 h of incubation, the medium were replaced with 100 μL of fresh medium in each well. Added 10 μL of CCK-8 reagent to each well and incubated at 37 ℃ for 2 h. Absorbance was measured at 450 nm using a microplate reader (SpectraMax 190, Molecular Devices, USA) [54].

Cellular uptake and uptake efficiency of PPD

For the visualization of the cellular uptake of nanoparticles, PEI-g-PEG was labeled with FITC (named $P^{FITC}P$). The $P^{FITC}PD$ was then incubated with OCM-1 cells, which were pre-seeded in cell culture slides at a density of 4×10^4 cells/well. After different times of co-culture with cells, cells were washed three times with cold PBS and the membranes were stained using DiI [55]. After washing with PBS, the Antifade Mounting Medium with DAPI was added and the coverslips were mounted on slides. Fluorescence channels were examined with a confocal laser scanning microscope (LSM 880, Zeiss, Germany). Also, flow cytometry was used to detect the effect of cellular uptake (BD FACS Calibur, Becton, Dickinson and Company, USA) [56].

Study on lysosome escape ability

As an important organelle for degrading substances from extracellular sources, lysosomes will degrade most nanomaterials, thereby interfering with the original therapeutic effect. The polycation material can avoid this phenomenon through the "proton sponge" effect, which is called lysosome escape [57]. Using the aforementioned cell seeding method (OCM-1 cells with 4×10^4 cells/well), the cells were fixed for 10 min, 30 min, 2 h, 6 h, 8 h, 12 h and 24 h after $P^{FITC}PDNA$ treatment, washed and used for lysosome staining. The Lyso-Tracker Red is a commonly used fluorescent dye that specifically accumulates in lysosomes due to its affinity for the acidic environment within lysosomes. The Lyso-Tracker Red was diluted to the working concentration (50 nM) in the culture medium. The cells were then incubated with the dye solution at 37 ℃ for 20 min. Seal the slide after washing away the floating color. The fluorescence signals of each channel were acquired under a confocal laser scanning microscope. The colocalization of the $P^{FITC}PDNA$ green signal and LT-Red signal (red) was recorded under the condition of keeping the same parameters.

In vitro gene transfection

The transfection experiment of the PPG (or PPshn) nanoparticles was carried out in HEK 293T cells and OCM-1 cells. The enhanced green fluorescent protein (GFP-pCAGGS) was used in this experiment as the reporter gene. Briefly, HEK 293T cells were seeded in a 24-well plate (4×10^4 cells/ well) and then cultured at 37 ℃ in 5% CO_2 overnight. The next day, the DMEM culture medium was firstly replaced with fresh DMEM with The PPG nanoparticles with various N/P ratios (5, 20, 30, 40) in each well, and the final concentration of DNA was 2, 3, 4 μg/mL, respectively. When incubated for 48 h, flow cytometry was used to detect the effect of HEK 293T cells on the green fluorescence expression in the normal cell group and the treated group.

The expression of GFP in OCM-1 cells (N/P=10) was also detected by flow cytometry. In addition, it was observed and recorded under an inverted fluorescence microscope. To better observe the cell transfection, the cells fixed with 4% paraformaldehyde were stained with lysosomal localization. After adding the Antifade Mounting Medium with DAPI, images of multiple fluorescence channels were recorded with a confocal laser scanning microscope.

Hypoxia-induced vasculogenic mimicry assay

OCM-1 cells were cultured under normoxia and hypoxia, respectively, and the cell growth status and tube-like structure formation were continuously observed. Briefly, OCM-1 cells were grown in 24-well plates at a density of 4×10^4 cells/well. After cell apposition, the cells were incubated in hypoxic (1% oxygen) and normoxic incubators, respectively. The fluid was changed once every 2–3 days and observed continuously. Brightfield images were taken using an inverted fluorescence microscope (Leica DMi8, Germany).

To detect the effect of oxygen levels on the proliferation of tumor cells at the DNA level, the EdU Cell Proliferation Kit with Alexa Fluor 488 was used. It was used for EdU labeling to detect proliferation [58]. In short, the cells were blocked and permeabilized for 20 min in 4% paraformaldehyde fix solution and enhanced immunostaining permeabilization buffer. Then the EdU was detected by the addition of Click reaction solution containing Alexa Fluor 488 azide for 30 min. Co-staining was performed with Hoechst 33,342 after EdU labeling, and the fluorescence signal was observed and counted.

Based on the adjustment of seeding plate density, OCM-1 cells were cultured under normoxic and hypoxic conditions as described above, and the medium containing PPshn nanoparticles was replaced with one containing PPshn nanoparticles after cell apposition, and the formation of tubular structures of tumor cells was continuously observed. The nuclei of each group of cells were stained on day 5 and photographed and recorded under the microscope.

Assessment of sequence fragment silencing efficacy

To screen the silencing effect of each sequence fragment, the expression of PDGFR-α protein was observed. After treatment with PPshn transfection, cells were fixed with 4% pre-cooled paraformaldehyde for 30 min. After subsequent PBS rinsing, 0.3% Triton X-100 permeabilization and 5% BSA closure, incubation with primary antibody (PDGFR-α) were performed overnight at 4 °C. After rinsing three times with PBS, samples were incubated with the secondary antibody for 1.5 h at room temperature. Antifade mounting medium with DAPI was added and the slices were blocked. Images of several individual fluorescence channels were recorded with a confocal laser scanning microscope (LSM 880, Zeiss, Germany).

Tube formation assay

To perform angiogenesis experiments on HUVECs, 96-well plates were first coated with growth factor-reduced Matrigel [59]. Briefly, 50uL Matrigel was added to each well and left in the incubator for 30 min before waiting for subsequent cell seeding of the plate. Cells were seeded at the density of 1×10^4 cells per well using 100 μL of conditioned medium (OCM-1 cell culture supernatant filtered through 220 nm). The continuous observation was then performed and photographic records were taken at different time points (4 h, 6 h, 8 h and 12 h). For the RNA interference group, HUVECs transfected with PPsh2 were grown as described above and subsequently compared with the control group.

Three-dimensional (3D) tumor culture assay

To evaluate the size of the tumor formed by the uveal melanoma cells, the uveal melanoma cells were transiently transfected as described above. To wells in a 96-well plate, 50 μL Matrigel was added and incubated for 30 min at 37 ℃. Subsequently, the transfected cells were inoculated in the plates and tumor formation was continuously observed over the following 24 h, where cells that had not been treated with transfection were observed as controls.

Analysis of EMT marker expression

In addition, the expression of the EMT marker E-Cadherin protein was examined. After being rinsed in PBS, the cells were permeabilized with 0.3% Triton X-100 and closed with 5% BSA, and then were incubated overnight at 4℃ with primary antibody (E-Cadherin). After rinsing three times with PBS, samples were incubated with secondary antibodies for 1.5 h at room temperature. Finally, fluorescence was observed under the microscope after labeling the nuclei with DAPI.

In vivo tumor assay

Animal models were used with 18–20 g BALB/C nude mice, screened to exclude those with congenital eye disease. In each group (randomly assigned by random number table), 10 nude mice from 2 independent experiments (5 nude mice in each independent experiment) were included. 2 μL cell suspension (containing 2×10^5 OCM-1 cells) was injected into the subretinal cavity of the right eye of each mouse. On the third day, the nude mice were randomly divided into two groups and injected with PBS and PPsh2 in the right eye, followed by slit lamp photography two weeks after injection. After euthanasia, all eyes were separated, weighed and fixed with a fixative solution (containing 10% formaldehyde, 40% ethanol and 10% acetic acid). The animal experiment was approved by the Experimental Animal Ethics Committee of Eye Hospital of Wenzhou Medical University.

The eyes were sagittally dissected and the internal tumor was observed under a stereoscopic microscope (SMZ18, Nikon, Japan). The tissue was then pathologically sectioned and set to a thickness of 5 μm and stained with hematoxylin-eosin stain (HE). In addition, the tissue sections were further stained with PAS and the shape of PAS-positive material connections was observed to determine the phenomenon of vasculogenic mimicry.

Statistical analysis

In the experiment, each sample included three to five replicates, and all data were expressed as the mean ± SD. GraphPad Prism 7(San Diego, California) was used for statistical analysis and one-way analysis of variance. The significance level was set at $p<0.05$. Differences with $p<0.05$ (*) were considered to be significant, those with $p<0.01$ (**) and $p<0.001$ (***) were considered to be very significant, and those with $p>0.05$ were considered to be nonsignificant. At $p=0.05$, the significance level was established. Differences with $p<0.05$ (*) were regarded as meaningful, those with $p<0.01$ (**) and $p<0.001$ (***) as extremely meaningful, and those with $p>0.05$ as nonsignificant.

Results and discussion

Preparation and characterization of gene polyplex

The gene polyplex's size varies above and below 150 nm when N/P is between 5 and 20, and its zeta potential is similarly around +30 mV, as shown in Fig. 1A. In particular, at N/P=10, the particle size was 153.2 ± 1.12694 nm, while the potential was 29.09333 ± 2.05583mV. The results demonstrate that cationic PEI-g-PEG can electrostatically condense negatively charged plasmid DNA into stable nanoparticles, which is required for efficient cellular uptake [60]. In a study by Olivia M. Merkel [61], the polymer and nucleic acid are mutually attracted via electrostatic interaction and subsequently self-assemble

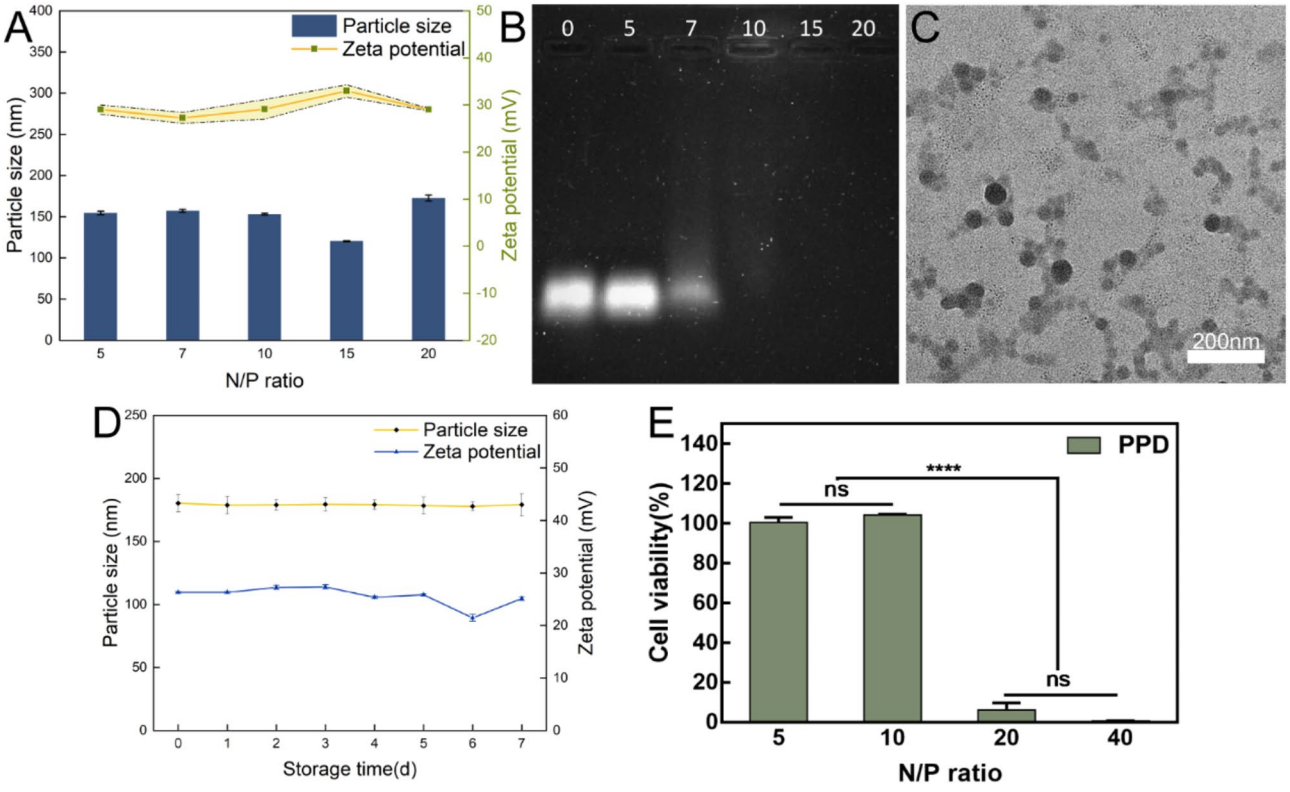

Fig. 1 Characterization and biocompatibility of gene nanoparticles. (**A**): Particle size and potential distribution of PPD polyplex under different N/P conditions. (**B**): The results of the agarose gel electrophoresis experiments corresponding to the above PPD polyplex are plotted. (**C**): TEM imaging of the PPD under the N/P ratio of ten. (**D**): Changes in particle size and Zeta potential of PPD (N/*P* = 10) for 7 days. (**E**): Cytotoxicity of PPD on OCM-1 under different N/P ratios

to form a nanostructure. The principle is essentially analogous to the interaction mechanism between PEI-g-PEG and plasmid DNA in this research. Both are founded on charge interaction to accomplish the construction of nanoparticles. Figure 1B demonstrates the ability of the PEI-g-PEG to encapsulate the gene fragments. As N/P increases, the brightness of the DNA bands gradually decreases. When N/*P*=7, some redundant billing fragments can still be detected, and when N/*P*=10, there is no band, indicating that under the condition of this ratio, the gene fragment is completely wrapped in the polyplex. The same is true for gene band detection with N/*P*>10. Figure 1C shows the morphology and distribution of gene nanoparticles when N/*P*=10. It can be seen that the size of the polyplex is less than 100 nm and it is spherical. Figure 1D shows that the size and electrical properties of PPD did not change significantly during 7 days, indicating great storage stability.

In vitro cytotoxicity evaluation

Figure 1E shows the effect of different N/P choices of PPD on OCM-1 cells while maintaining the same nucleic acid concentration. It can be seen that when N/P is less than 10, the cells remain in a good cellular state, while when N/P is greater than 20, the cells are more toxic. Therefore, subsequent transfection experiments should consider the N/P ratio carefully.

Analysis of cellular uptake efficiency

The efficiency of cellular internalization of gene nanoparticles by tumor cells is the basis for subsequent RNA interference treatment [62]. Figure 2A shows the fluorescence signal recorded at various time points after co-incubation of P^{FITC}PDNA with OCM-1 cells over a 24 h period. It can be seen that the green fluorescence (P^{FITC}P-DNA) gradually accumulates over time. After 30 min, the green stain adhered to the cell membrane surface (red) and gave a yellow signal, after 4 h labeled nanoparticles were found inside the individual cytoplasm, and after 24 h the cells were covered in green. Figure 2B shows the statistical data of cell fluorescence signals at different time points. The green fluorescence of the cells gradually increased with the prolongation of the incubation time, and the fluorescence intensity leveled off after 2 h, which indicates that the absorption of gene polymers by OCM −1 gradually reached a saturation level. Figure 2C shows that after 4 h of co-culture, 98.9% of OCM-1 cells detected by flow cytometry had a green fluorescent

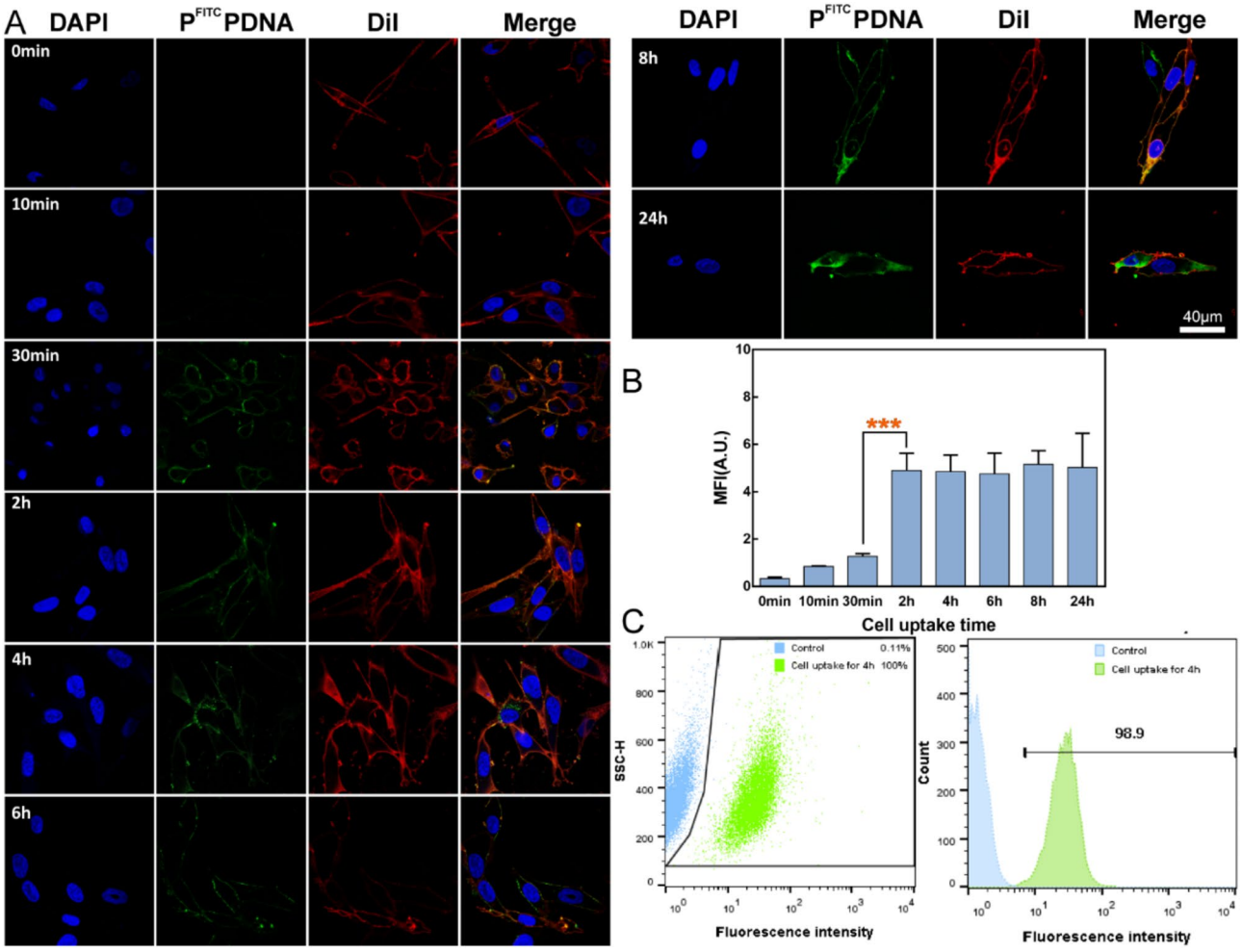

Fig. 2 Analysis of cellular uptake capacity. (**A**): Representative images of OCM-1 cells uptake of P^{FITC}PDNA nanoparticles at different time points. Blue signal: nucleus, DAPI. Red signal: cell membrane, DiI. Green signal: P^{FITC}PDNA, nanoparticles. (**B**): Quantitative statistics of cell uptake fluorescence in Figure A. (**C**): Flow cytometry results of OCM-1 cells after 4 h uptake of P^{FITC}PDNA nanoparticles

signal, which may be due to the adherence or uptake of the P^{FITC}PDNA polyplex by almost all cells. These results indicated that OCM-1 cells have an excellent ability to internalize P^{FITC}PDNA nanoparticles, which facilitates the subsequent transfection process. Similar to numerous other studies in the field of gene delivery, such as the research reported in a study by Abdul Hakeem [63], the overarching principle remains unaltered: the efficient internalization of nanoparticle carriers is a prerequisite for effective transfection.

Lysosomal escape capacity analysis

Most nanocarriers enter cells through the endocytic pathway, and when endosomes mature through acidification and invade lysosomes, the loaded drugs or genes are destroyed by digestive enzymes, which is one of the major challenges in the process of gene therapy [64]. Therefore, the ability of nanocarriers to escape lysosomes is critical for the delivery. Figure 3 shows that after 24 h of continuous observation, the green signal from the P^{FITC}PDNA polyplex gradually increased, while the red signal from the labeled lysosome gradually decreased. After 6 h of incubation, a yellow signal from P^{FITC}PDNA superimposed on LT-Red appears. The yellow signal gradually increases at 6–12 h, while the red signal basically disappears at 24 h (due to the disruption of lysosomes), and the green signal is distributed around the blue nucleus (DAPI) and in the cytoplasm. It is highly evident that PEI-g-PEG exhibits remarkable capabilities in safeguarding nucleic acids from degradation by lysosomes. This unique polymer-based carrier forms stable polyplex with nucleic acids through electrostatic interactions and other molecular forces [65]. Once these polyplex are internalized by cells, they are trafficked through the endocytic pathway. During this process, lysosomes, which are the cellular organelles responsible for degrading various macromolecules, attempt to break down the incoming polyplex. However, due to the protective

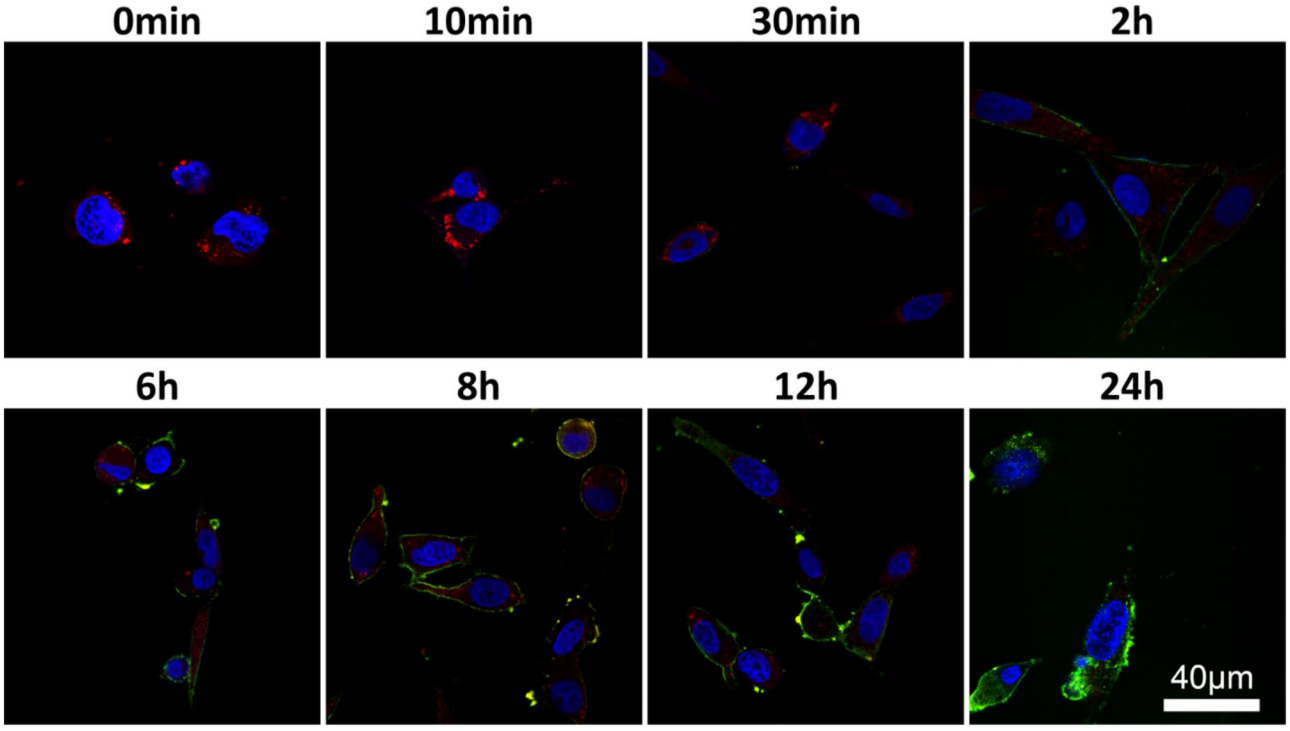

Fig. 3 Fluorescence signal recording of P^{FITC}PDNA at different time points during the lysosomal escape in OCM-1 cells. Blue signal: nucleus, DAPI. Red signal: lysosome, LT-Red. Green signal: P^{FITC}PDNA, nanoparticles

properties of PEI-g-PEG, it effectively shields the nucleic acids from the harsh lysosomal environment, preventing the hydrolytic enzymes within lysosomes from acting on the nucleic acids and causing their degradation. As a result of this protection, the nucleic acids remain intact and are able to reach their intended cellular destinations.

In vitro gene transfection

Figure 4 show transfection attempts using PPG in HEK 293T cells. As shown in Fig. 4A, the transfection efficiency gradually increased with the amount of delivered plasmid. In the case of the same plasmid quality, the transfection rate gradually increased when $N/P<20$, and decreased gradually when $N/P>20$. As shown in Fig. 4B, the curved surface in the figure is the transfection surface simulated by each flow statistic in 4A, while the plane is the cell viability after treatment in HEK 293T cells. The curved surface below the plane is suitable for transfection conditions for subsequent experiments. To maintain maximum transfection efficiency, the N/P ratio should be less than 20 when the package mass is 4 μg.

Figure 5 shows the transfection effect and efficiency of 4 μg plasmid DNA (GFP-pCAGGS) in OCM-1 cells at $N/P=10$. As shown in Fig. 5A, this condition allowed the successful transfection of OCM-1 cells with GFP. Figure 5B shows that the transfection efficiency reached 26.7%. Figure 5C shows that both green fluorescent protein and red lysosomes are located in the cytoplasm of cells from the observation of microstructure.

Hypoxia-induced vasculogenic mimicry assay

Figure 6A shows that there was no significant difference in the growth status of the two groups of cells incubated at the two oxygen concentrations for 1 day. On the 4th day of culture, channel-like vacant areas appeared in the cell arrays of both groups. Whereas, cells under hypoxic conditions appeared to have a clear blank area on day 8, while cells under normoxic conditions covered the entire well. On day 9, this phenomenon was even more pronounced, with the cells in the center of the plate showing multiple layers of growth and clear vasculogenic mimicry. Aging cells and lamellar structures can be seen in the periphery. In contrast, the cells remained packed throughout the wells under normoxic conditions. The following reasons may account for such results. Firstly, hypoxia can activate the hypoxia-inducible factor (HIF) [66]. This activated HIF-1 is able to promp tumor cells to form vascular-like structures. Secondly, the plasticity of tumor cells themselves is enhanced under the hypoxic environment. Some tumor cells acquire endothelial cell-like characteristics and can express endothelial cell-related markers, such as CD31 and so on [67]. At the same time, the intercellular connections become loose and new connection modes appear, enabling tumor cells to connect with each other like vascular endothelial cells

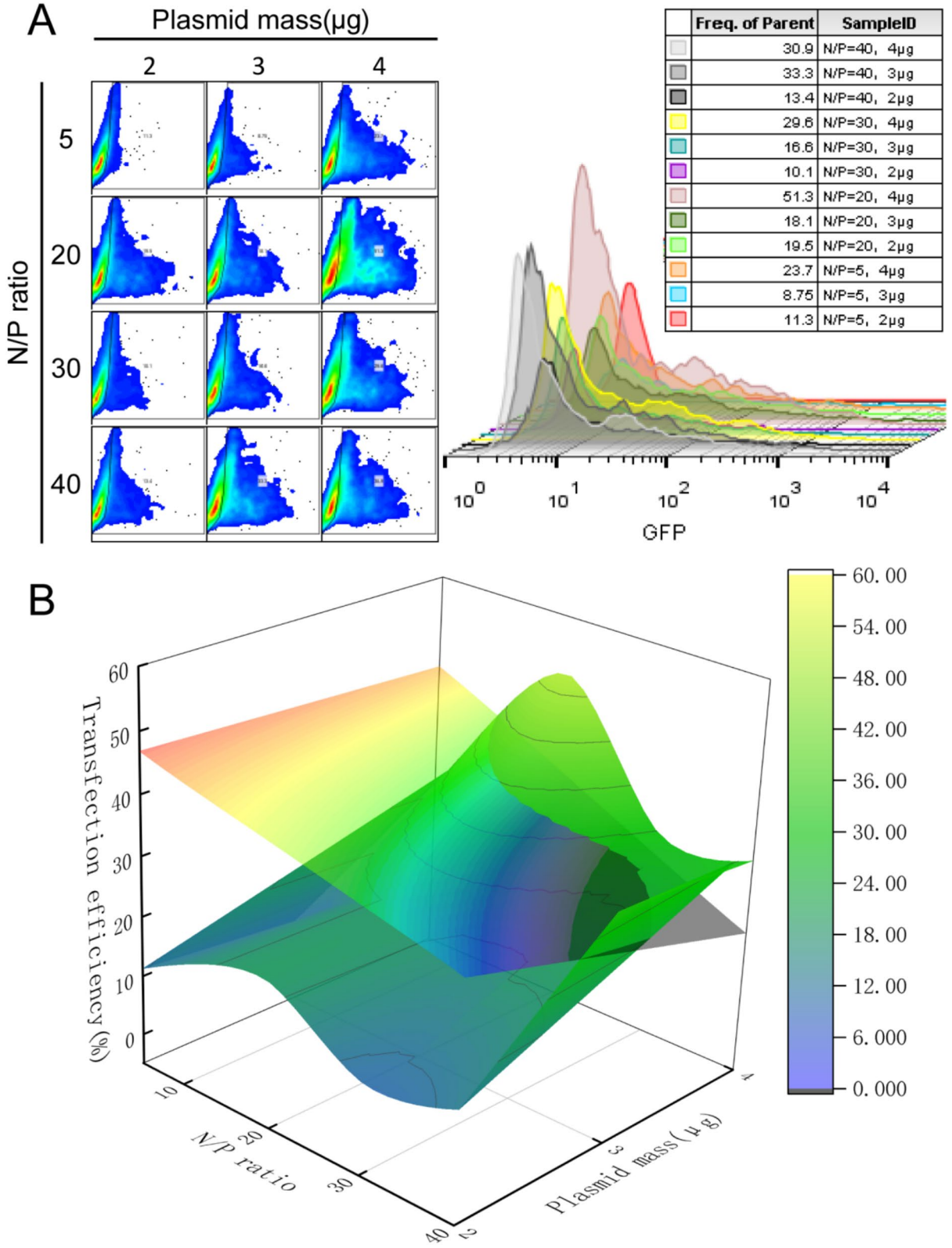

Fig. 4 Screening of transfection conditions. (**A**): Flow cytometry results of transfection in HEK 293T cells with different N/P ratios and plasmid content. (**B**): Comprehensive Consideration Diagram of the Survival and Transfection Status of HEK 293T Cells under Various Conditions after Transfection Treatment

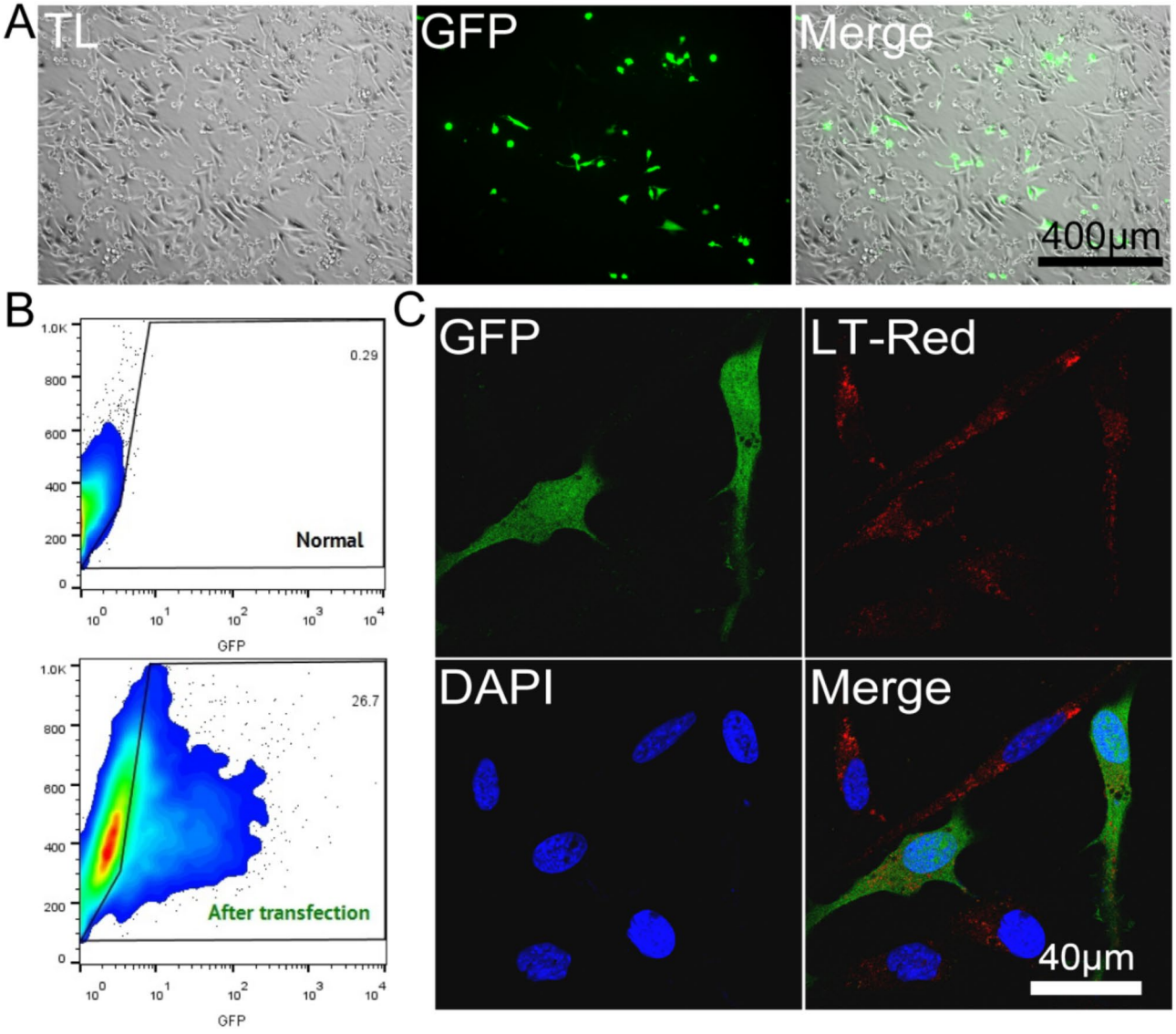

Fig. 5 Transfection ability of polymers. (**A**): Effect of PPG transfection on green fluorescent protein in OCM-1 cells. TL: The transmission light mode of a microscope represents the bright - field. (**B**): Transfection efficiency of green fluorescent protein in OCM-1 cells. C: Microscopic observation of green fluorescent protein expression in OCM-1 cells. LT-Red: Lyso-Tracker Red

and form the basic structure of vascular-like channels, providing important conditional support for the growth and metastasis of tumors. Figure 6B shows the proliferation capacity at the DNA level after 9 days of incubation. Under hypoxic conditions, pale green fluorescence was visible in the central and peripheral parts of the plate (especially in the four walls of the vascular-like channels). Under normal oxygen conditions, green fluorescence was weakly positive or even negative at several positions. Fluorescence was quantified as shown in Fig. 6C. The total cell count (Hoechst) of the normoxia group was significantly higher than that of the hypoxia group, but the DNA level proliferation of the hypoxia group was more active than that of the normoxia group.

The same seeding plate density and observation period were adjusted for vasculogenic mimicry interference experiments. As shown in Fig. 7A, the phenomenon of angiogenesis mimicry was evident in the blank group (without any treatment group) under hypoxia. However, this phenomenon was significantly suppressed after treatment with PPshn, suggesting that four interfering fragment sequences have different roles. In Fig. 7B, it shows the expression of intracellular proteins after treatment with four gene polymers (PEI-g-PEG encapsulating four PDGFR-α shRNA fragments) during the process of hypoxia-induced tumor cells to form vasculogenic mimicry. Herein, the RFP (red fluorescent protein) is derived from the mCherry coding sequence encoding the red

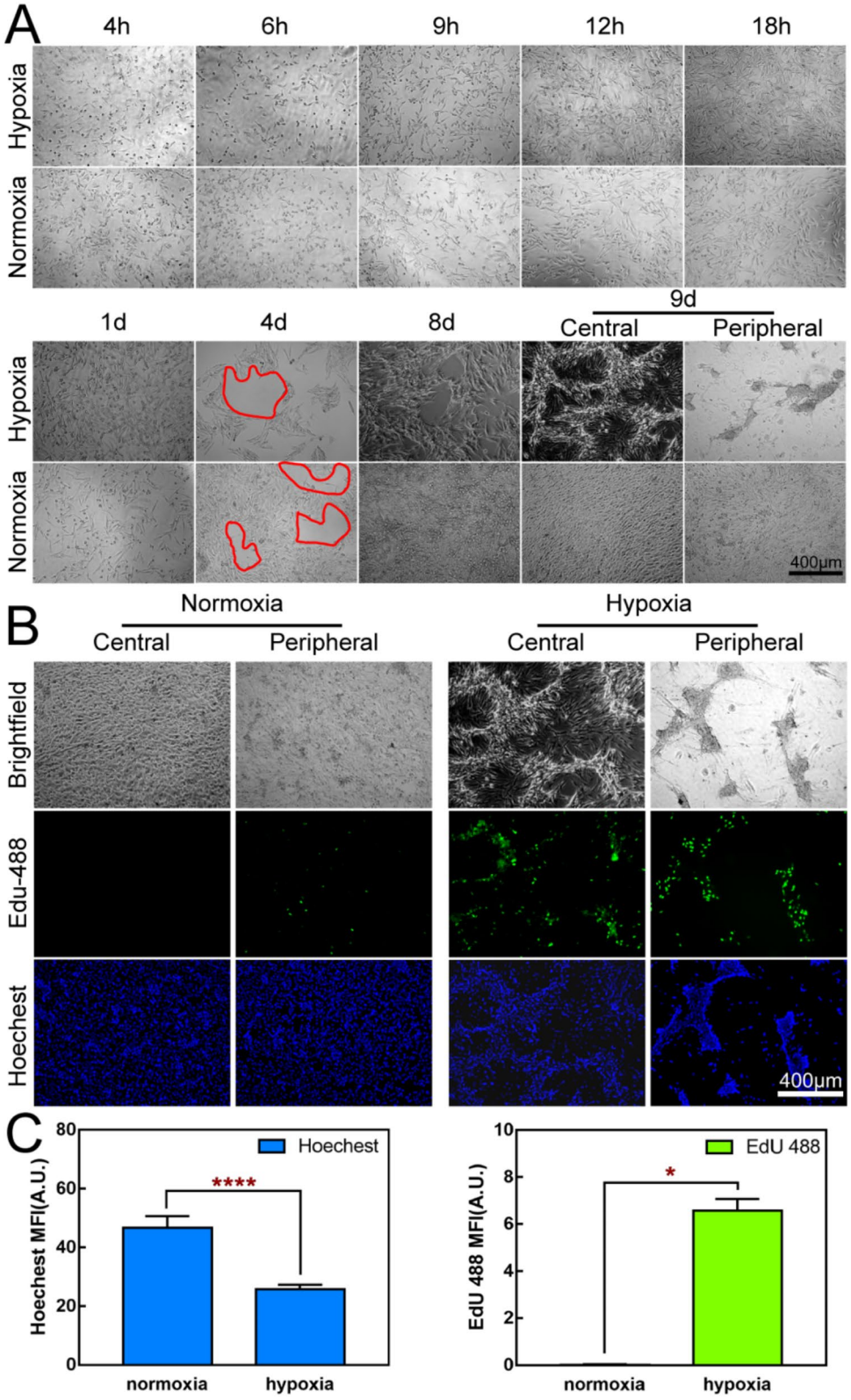

Fig. 6 Hypoxia-Induced Vasculogenic Mimicry. (**A**): Hypoxia-induced vasculogenic mimicry in OCM-1 cells. (**B**): Effect of hypoxia on cell proliferation. Edu-488: Green fluorescence, newly synthesized DNA. Hoechst: Blue fluorescence, cell nucleus. (**C**): Quantitative immunofluorescence statistics in Fig. 6B

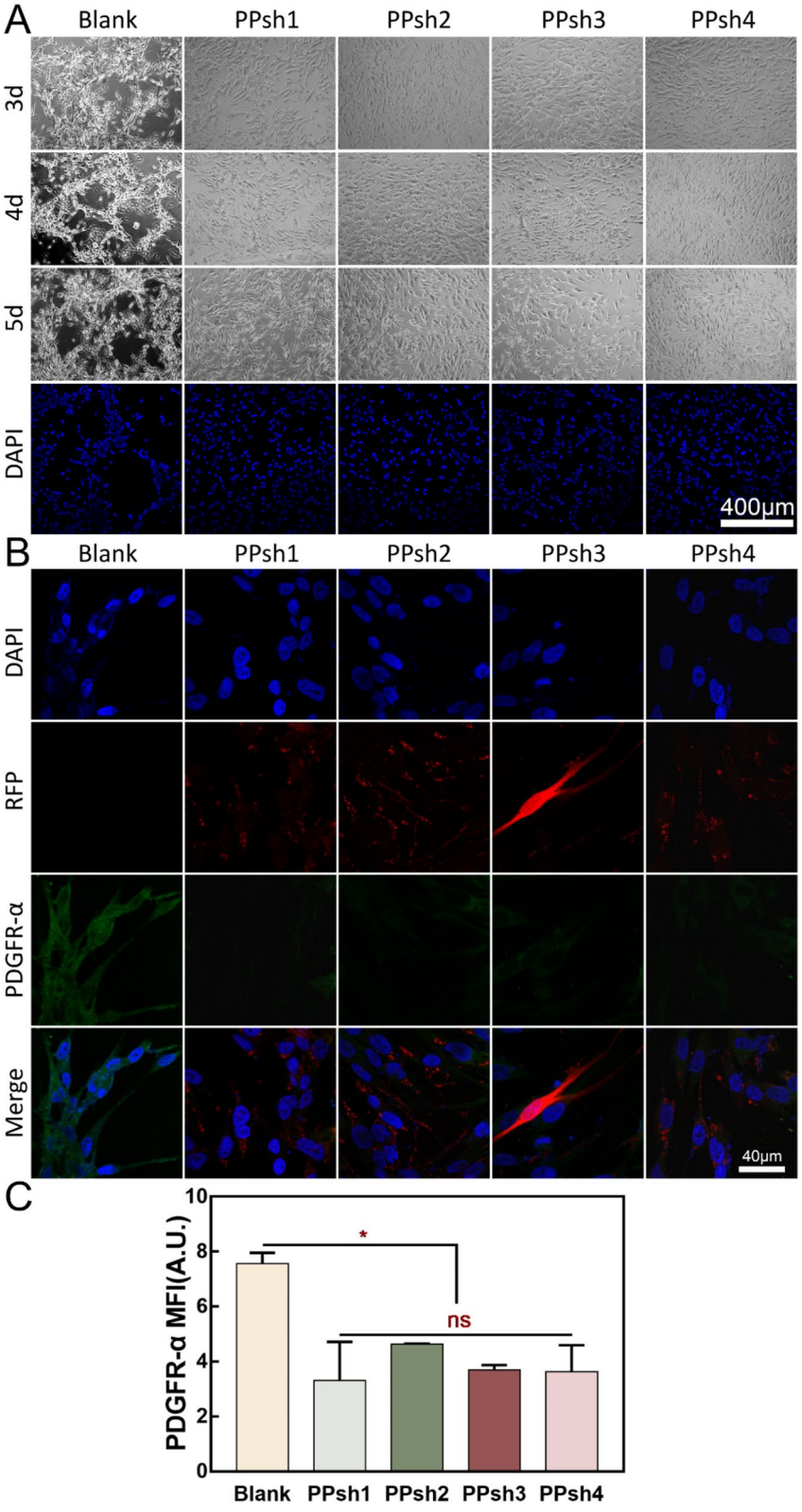

Fig. 7 Evaluation of the Ability to Inhibit Vasculogenic Mimicry. (**A**): Interference results of four different PDGFR-α-shRNA sequences (PPshn) on vasculogenic mimicry. (**B**): Immunofluorescence analysis of targeting silencing protein (PDGFR-α) in OCM-1 cells. RFP: The red fluorescent protein encoded by mCherry. PDGFR-α: The PDGFR-α protein after immunofluorescent staining (with the secondary antibody carrying green fluorescence). DAPI: Nucleus. (**C**): Quantitative immunofluorescence analysis of PDGFR-α protein in Fig. 7B

fluorescent protein within the gene fragment, which can serve as an indirect indication of the successful transfection of the gene fragment. Simultaneously, the green fluorescence represents the immunofluorescent staining of the intracellular PDGFR-α protein. Evidently, in the untreated group (blank group), following hypoxia induction, the tumor cells express the PDGFR-α protein. In the treatment groups (PPsh1–4 groups), each gene polymer was successfully transfected (as evidenced by the successful expression of the red protein), and concomitantly, the expression of the PDGFR-α protein was attenuated to varying degrees (manifested by the weakened green signal). In conjunction with the results of Fig. 7A, it can be corroborated that during the process of interfering with the generation of the vasculogenic mimicry phenomenon, it is likely influenced by the reduction in the synthesis of the PDGFR-α protein. Simultaneously, quantitative fluorescence statistics were performed and Fig. 7C shows that there was no significant difference between the treatment groups, while there was a significant difference with the blank group. These results indicated that the four interfering fragments inhibited the production of PDGFR-α protein to varying degrees, and PEI-g-PEG could indeed be used as a non-viral gene vector for the delivery of nucleic acid fragments.

Tube formation assay

Tumor cells secrete large amounts of pro-angiogenic factors to promote angiogenesis during tumor development [68]. Figure 8A shows that OCM-1 cell culture supernatant significantly induces the formation of reticular vasculature in HUVEC cells. At 6 h, HUVEC cells tended to be arranged in an orderly manner, and at 8 h, they formed the prototype of the reticular structure, and at 12 h, the phenomenon was most obvious. In contrast, PPsh2-transfected HUVEC cells showed no tendency to form tubes.

Three-dimensional (3D) tumor culture assay

As shown in Fig. 8B, OCM-1 cells gradually migrated to form clusters of tumor cells on the surface of Matrigel, especially after 24 h. The cells in the OCM-1 cell group transfected with PPsh2 migrated in clusters, but the size of the clusters was significantly smaller than that in the non-transfected cell group (OCM-1 + PPsh2).

To further assess the inhibitory effect on tumorigenesis, we examined the expression of the EMT marker E-cadherin in cell clusters. As shown in Fig. 8C, the red signal of the E-cadherin marker was significantly lower in untreated OCM-1 cells than in the group treated with PPsh2-transfected OCM-1 cells. Upregulation of E-cadherin indicated that intercellular adhesion persisted after transfection and significantly reduced the risk of tumor cell metastasis [69]. The newly synthesized E-cadherin protein will rapidly be localized to the cell surface and bind to the E-cadherin molecules of adjacent cells through its extracellular domain, forming stable homodimers or heterodimers and thereby strengthening the adherens junctions between cells. This tight intercellular adhesion is like a series of sturdy "city walls", preventing tumor cells from detaching from the primary tumor site. Since the metastasis of tumor cells often requires breaking through the intercellular connection restraints, and the upregulation of E-cadherin makes this breakthrough more difficult, thus significantly reducing the risk of tumor cell metastasis [70]. This also confirmed that the EMT process was inhibited after PPsh2 treatment.

In vivo tumor detection

Figure 9A shows gross pictures, slit lamps, eye sections and HE staining of pathological sections of nude mice. In the Blank group, the eyes were clear and translucent, both with the naked eye and slit lamp, and the vitreous cavity was clear of foreign bodies on gross observation. In the OCM-1 + PBS group, the slit lamp showed a clear white pupil, and the gross section of the eye showed tumor tissue filling the entire vitreous cavity and adhering to the surface of the lens. In the OCM-1 + PPsh2 group, slight white pupils could be seen in the eyes of nude mice, and smaller tumor tissues under the retina were visible in the eye dissection. The whole-eye HE staining corresponds to the gross view of the eye. In the Blank group, the intraocular tissues were intact, while in the OCM-1 + PBS group, OCM-1 was seen to fill the subretinal cavity and enter the vitreous cavity near the oar serrata part, and the cells adhered to the lens surface while the tumor tissue squeezed the lens. In the OCM-1 + PPsh2 group, HE staining revealed smaller tumor growth in the subretinal space, which was significantly different from the OCM-1 + PBS group.

Figure 9B shows weight statistics for isolated eyes. It can be seen that the eye weight of the OCM-1 + PPsh2 group was significantly lower than that of the OCM-1 + PBS group. Figure 9C shows that PAS staining in the OCM-1 + PBS group revealed interconnected ring-like network channels (marked by yellow arrows in Fig. 9C1), whereas this phenomenon was significantly reduced in the OCM-1 + PPsh2 group (Fig. 9C2). Thus, PPsh2 treatment significantly reduced the formation of blood vessel-like channels and greatly limited tumor growth.

Conclusion

In this study, gene nanoparticles with PEI-g-PEG as a nonviral vector were prepared by electrostatic conjugation to deliver targeted interfering fragments to OCM-1 cells against the EMT process mediated by PDGFR-α, and achieved tumor reduction. PEI-g-PEG can fully wrap

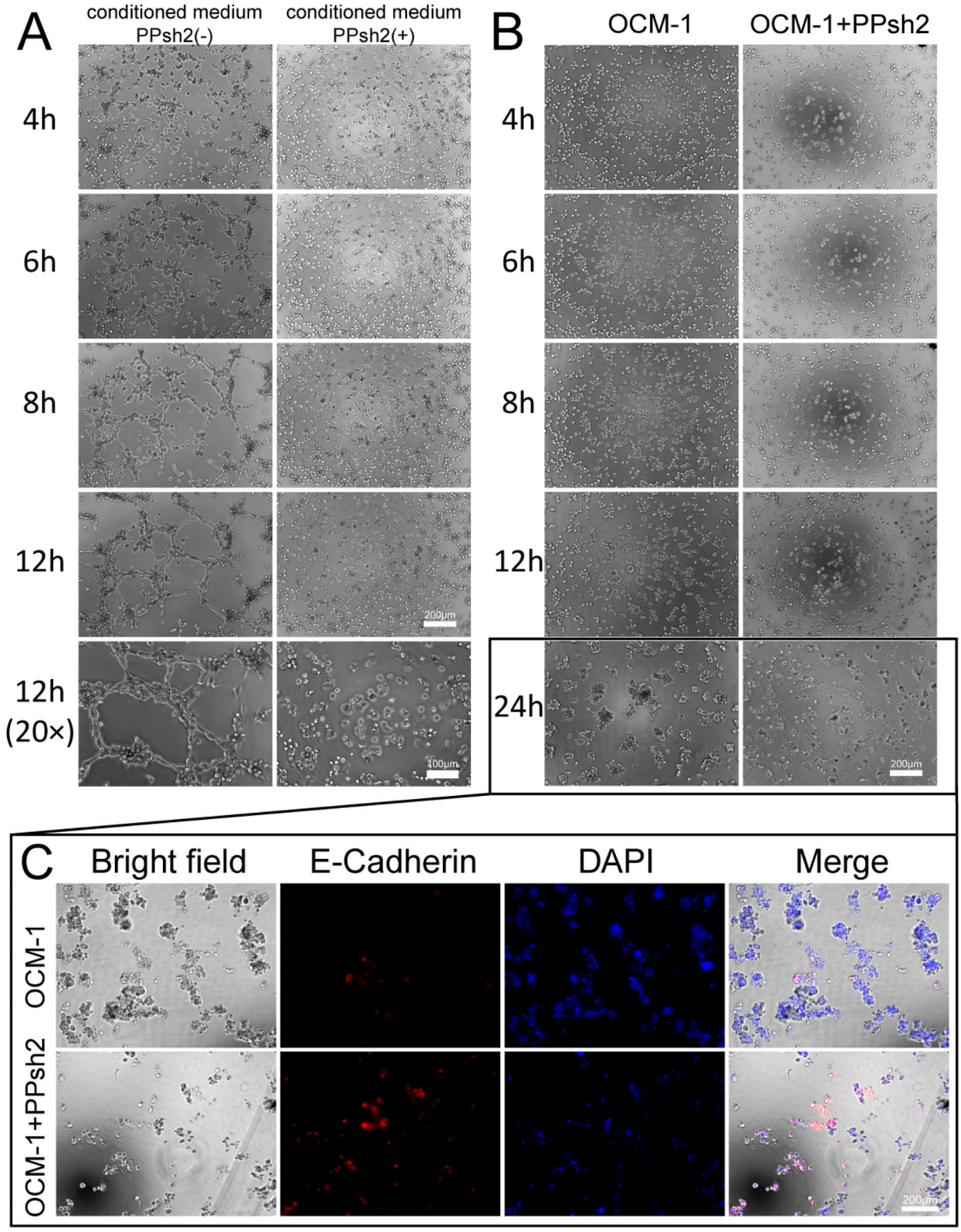

Fig. 8 Evaluation of Anti-tumor Effects. (**A**): Establishment of tube formation model and the interference effects of PPsh2. (**B**): Three-dimensional tumorigenesis and interference effects of PPsh2. (**C**): Immunofluorescence analysis of the EMT marker E-Cadherin protein in Fig. 8B. DAPI: Nucleus. E-Cadherin: The E-Cadherin protein after immunofluorescent staining (with the secondary antibody carrying red fluorescence)

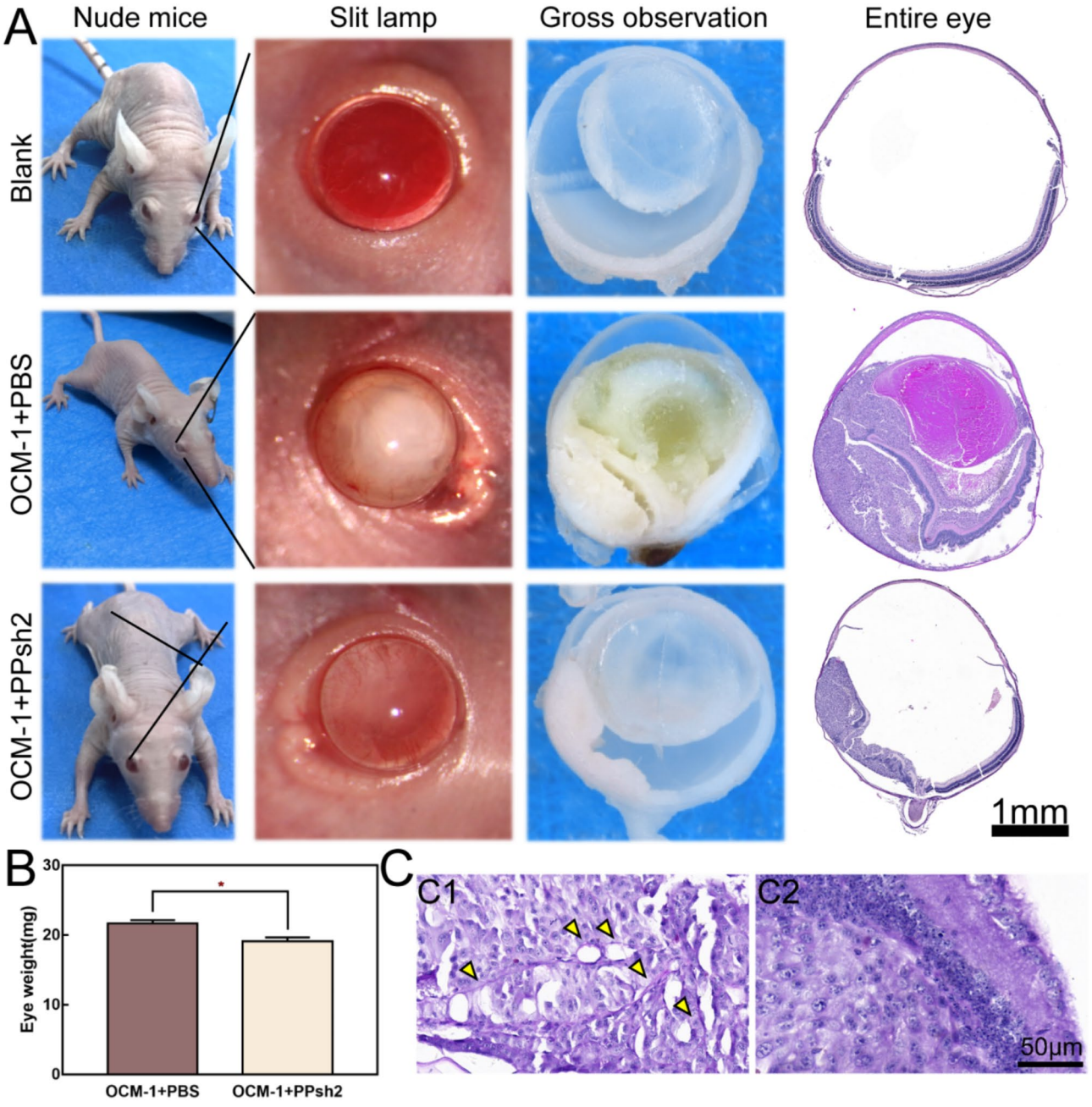

Fig. 9 Establishment of in vivo tumor models and evaluation of inhibitory effects. (**A**): Gross pictures, slit lamps, eye sections and pathological sections of nude mice were stained with HE. Blank: the group of healthy nude mouse. OCM-1 + PBS: the group of tumor modeling. OCM-1 + PPsh2: the group of treatment by PPsh2. (**B**): Eye Weight Statistics. (**C**): PAS staining analysis

nucleic acid fragments when N/P is 10, and have a small nanometer size, positive potential, and excellent biocompatibility. The nanoparticles achieved 98.9% uptake efficiency within 4 h of co-incubation with the cells, and within 24 h the nucleic acids could evade lysosomal degradation by distending the lysosomes to exert their normal therapeutic effects. The nanoparticles showed good transfection effects in both HEK 293T cells and OCM-1 cells. It also inhibited the vasculogenic mimicry of OCM-1 cells under hypoxic conditions and effectively interfered with the production of the targeted PDGFR-α protein. Furthermore, PPsh2 inhibited tumor supernatant-induced angiogenesis and reduced tumor cell migration and cell clump growth induced by E-cadherin degradation. In vivo animal studies have shown that PPsh2 has a beneficial inhibitory effect on UM growth and reduces the formation of blood vessel-like channels. Therefore, PEI-g-PEG could be an excellent nonviral gene

therapy vector, and PDGFR-α could serve as a potential target to modulate EMT-associated vasculogenic mimicry and migration phenomena, as a new way to improve therapeutic management of uveal melanoma.

Acknowledgements
Not applicable.

Author contributions
Jiahao Wang: Investigation, Data curation, Methodology, Formal analysis, Writing - original draft. Zhirong Chen: Investigation, Validation. Peiyi Zhao: Investigation. Yajia Wang: Investigation. Jiang Chen: Investigation. Quankui Lin: Conceptualization, Funding acquisition, Project administration, Resources, Supervision, Writing-review & editing. All authors reviewed the manuscript.

Funding
This work was financially supported by the Zhejiang Provincial Natural Science Foundation [LR23H180001].

Data availability
No datasets were generated or analysed during the current study.

Declarations

Ethics approval and consent to participate
The animal experiment was approved by the Experimental Animal Ethics Committee of Eye Hospital of Wenzhou Medical University.

Consent for publication
Not applicable.

Competing interests
The authors declare no competing interests.

Received: 5 September 2024 / Accepted: 17 December 2024
Published online: 26 December 2024

References

1. Zhang J, Liu S, Ye Q, Pan J. Transcriptional inhibition by CDK7/9 inhibitor SNS-032 abrogates oncogene addiction and reduces liver metastasis in uveal melanoma. Mol Cancer. 2019;18(1):140. https://doi.org/10.1186/s12943-019-1070-7.
2. Chen X, Wu Q, Depeille P, Chen P, Thornton S, Kalirai H, Coupland SE, Roose JP, Bastian BC. RasGRP3 mediates MAPK pathway activation in GNAQ Mutant Uveal Melanoma. Cancer Cell. 2017;31(5):685–e6966. https://doi.org/10.1016/j.ccell.2017.04.002.
3. Dong L, You S, Zhang Q, Osuka S, Devi NS, Kaluz S, Ferguson JH, Yang H, Chen G, Wang B, Grossniklaus HE, Van Meir EG. Arylsulfonamide 64B inhibits Hypoxia/HIF-Induced expression of c-Met and CXCR4 and reduces primary Tumor Growth and Metastasis of Uveal Melanoma. Clin Cancer Res. 2019;25(7):2206–18. https://doi.org/10.1158/1078-0432.CCR-18-1368.
4. Li P, He J, Yang Z, Ge S, Zhang H, Zhong Q, Fan X. ZNNT1 long noncoding RNA induces autophagy to inhibit tumorigenesis of uveal melanoma by regulating key autophagy gene expression. Autophagy. 2020;16(7):1186–99. https://doi.org/10.1080/15548627.2019.1659614.
5. Robertson AG, Shih J, Yau C, Gibb EA, Oba J, Mungall KL, Hess JM, Uzunangelov V, Walter V, Danilova L, Lichtenberg TM, Kucherlapati M, Kimes PK, Tang M, Penson A, Babur O, Akbani R, Bristow CA, Hoadley KA, Iype L, Chang MT, Network TR, Cherniack AD, Benz C, Mills GB, Verhaak RGW, Griewank KG, Felau I, Zenklusen JC, Gershenwald JE, Schoenfield L, Lazar AJ, Abdel-Rahman MH, Roman-Roman S, Stern MH, Cebulla CM, Williams MD, Jager MJ, Coupland SE, Esmaeli B, Kandoth C, Woodman SE. Integrative analysis identifies four molecular and clinical subsets in Uveal Melanoma. Cancer Cell. 2017;32(2):204–e22015. https://doi.org/10.1016/j.ccell.2017.07.003.
6. Mathivet T, Bouleti C, Van Woensel M, Stanchi F, Verschuere T, Phng LK, Dejaegher J, Balcer M, Matsumoto K, Georgieva PB, Belmans J, Sciot R, Stockmann C, Mazzone M, De Vleeschouwer S, Gerhardt H. Dynamic stroma reorganization drives blood vessel dysmorphia during glioma growth. EMBO Mol Med. 2017;9(12):1629–45. https://doi.org/10.15252/emmm.201607445.
7. Linkous A, Geng L, Lyshchik A, Hallahan DE, Yazlovitskaya EM. Cytosolic phospholipase A2: targeting cancer through the tumor vasculature. Clin Cancer Res. 2009;15(5):1635–44. https://doi.org/10.1158/1078-0432.CCR-08-1905.
8. Mak MP, Tong P, Diao L, Cardnell RJ, Gibbons DL, William WN, Skoulidis F, Parra ER, Rodriguez-Canales J, Wistuba II, Heymach JV, Weinstein JN, Coombes KR, Wang J, Byers LA. A Patient-Derived, Pan-cancer EMT signature identifies global molecular alterations and Immune Target Enrichment following epithelial-to-mesenchymal transition. Clin Cancer Res. 2016;22(3):609–20. https://doi.org/10.1158/1078-0432.CCR-15-0876.
9. Pastushenko I, Brisebarre A, Sifrim A, Fioramonti M, Revenco T, Boumahdi S, Van Keymeulen A, Brown D, Moers V, Lemaire S, De Clercq S, Minguijón E, Balsat C, Sokolow Y, Dubois C, De Cock F, Scozzaro S, Sopena F, Lanas A, D'Haene N, Salmon I, Marine J-C, Voet T, Sotiropoulou PA, Blanpain C. Identification of the tumour transition states occurring during EMT. Nature. 2018;556(7702):463–8. https://doi.org/10.1038/s41586-018-0040-3.
10. Jolly MK, Somarelli JA, Sheth M, Biddle A, Tripathi SC, Armstrong AJ, Hanash SM, Bapat SA, Rangarajan A, Levine H. Hybrid epithelial/mesenchymal phenotypes promote metastasis and therapy resistance across carcinomas. Pharmacol Ther. 2019;194:161–84. https://doi.org/10.1016/j.pharmthera.2018.09.007.
11. Shen T, Cai LD, Liu YH, Li S, Gan WJ, Li XM, Wang JR, Guo PD, Zhou Q, Lu XX, Sun LN, Li JM. Ube2v1-mediated ubiquitination and degradation of Sirt1 promotes metastasis of colorectal cancer by epigenetically suppressing autophagy. J Hematol Oncol. 2018;11(1):95. https://doi.org/10.1186/s13045-018-0638-9.
12. Yang XG, Zhu LC, Wang YJ, Li YY, Wang D. Current advance of therapeutic agents in clinical trials potentially targeting Tumor plasticity. Front Oncol. 2019;9:887. https://doi.org/10.3389/fonc.2019.00887.
13. Marcucci F, Stassi G, De Maria R. Epithelial-mesenchymal transition: a new target in anticancer drug discovery. Nat Rev Drug Discov. 2016;15(5). https://doi.org/10.1038/nrd.2015.13. 311 – 25.
14. Lakshmikanthan S, Sobczak M, Chun C, Henschel A, Dargatz J, Ramchandran R, Chrzanowska-Wodnicka M. Rap1 promotes VEGFR2 activation and angiogenesis by a mechanism involving integrin alphavbeta(3). Blood. 2011;118(7):2015–26. https://doi.org/10.1182/blood-2011-04-349282.
15. Stahl PJ, Chan TR, Shen YI, Sun G, Gerecht S, Yu SM. Capillary Network-Like Organization of endothelial cells in PEGDA Scaffolds Encoded with angiogenic signals via Triple Helical hybridization. Adv Funct Mater. 2014;24(21):3213–25. https://doi.org/10.1002/adfm.201303217.
16. Qu Y, Chen Q, Lai X, Zhu C, Chen C, Zhao X, Deng R, Xu M, Yuan H, Wang Y, Yu J, Huang J. SUMOylation of Grb2 enhances the ERK activity by increasing its binding with Sos1. Mol Cancer. 2014;13:95. https://doi.org/10.1186/1476-4598-13-95.
17. Boosani CS, Mannam AP, Cosgrove D, Silva R, Hodivala-Dilke KM, Keshamouni VG, Sudhakar A. Regulation of COX-2 mediated signaling by alpha3 type IV noncollagenous domain in tumor angiogenesis. Blood. 2007;110(4):1168–77. https://doi.org/10.1182/blood-2007-01-066282.
18. Maroufi NF, Amiri M, Dizaji BF, Vahedian V, Akbarzadeh M, Roshanravan N, Haiaty S, Nouri M, Rashidi MR. Inhibitory effect of melatonin on hypoxia-induced vasculogenic mimicry via suppressing epithelial-mesenchymal transition (EMT) in breast cancer stem cells. Eur J Pharmacol. 2020;881:173282. https://doi.org/10.1016/j.ejphar.2020.173282.
19. Reece KM, Richardson ED, Cook KM, Campbell TJ, Pisle ST, Holly AJ, Venzon DJ, Liewehr DJ, Chau CH, Price DK, Figg WD. Epidithiodiketopiperazines (ETPs) exhibit in vitro antiangiogenic and in vivo antitumor activity by disrupting the HIF-1alpha/p300 complex in a preclinical model of prostate cancer. Mol Cancer. 2014;13:91. https://doi.org/10.1186/1476-4598-13-91.
20. Lee D, Yu JS, Ha JW, Lee SR, Lee BS, Kim JC, Kim JK, Kang KS, Kim KH. Antitumor potential of Withanolide glycosides from Ashwagandha (Withania somnifera) on apoptosis of Human Hepatocellular Carcinoma Cells and tube formation in human umbilical vein endothelial cells. Antioxid (Basel). 2022;11(9):1761. https://doi.org/10.3390/antiox11091761.
21. Moser JC, Pulido JS, Dronca RS, McWilliams RR, Markovic SN, Mansfield AS. The Mayo Clinic experience with the use of kinase inhibitors, ipilimumab, bevacizumab, and local therapies in the treatment of metastatic uveal melanoma. Melanoma Res. 2015;25(1):59–63. https://doi.org/10.1097/CMR.0000000000000125.
22. Piperno-Neumann S, Diallo A, Etienne-Grimaldi MC, Bidard FC, Rodrigues M, Plancher C, Mariani P, Cassoux N, Decaudin D, Asselain B, Servois V. Phase II trial of Bevacizumab in Combination with Temozolomide as First-Line

treatment in patients with metastatic uveal melanoma. Oncologist. 2016;21(3):281–2. https://doi.org/10.1634/theoncologist.2015-0501.
23. Fane ME, Ecker BL, Kaur A, Marino GE, Alicea GM, Douglass SM, Chhabra Y, Webster MR, Marshall A, Colling R, Espinosa O, Coupe N, Maroo N, Campo L, Middleton MR, Corrie P, Xu X, Karakousis GC, Weeraratna AT. sFRP2 supersedes VEGF as an age-related driver of Angiogenesis in Melanoma, affecting response to Anti-VEGF therapy in older patients. Clin Cancer Res. 2020;26(21):5709–19. https://doi.org/10.1158/1078-0432.CCR-20-0446.
24. Francis JH, Kim J, Lin A, Folberg R, Iyer S, Abramson DH. Growth of Uveal Melanoma following Intravitreal Bevacizumab. Ocul Oncol Pathol. 2017;3(2):117–21. https://doi.org/10.1159/000450859.
25. Kang X, Xu E, Wang X, Qian L, Yang Z, Yu H, Wang C, Ren C, Wang Y, Lu X, Xia X, Guan W, Qiao T. Tenascin-c knockdown suppresses vasculogenic mimicry of gastric cancer by inhibiting ERK- triggered EMT. Cell Death Dis. 2021;12(10):890. https://doi.org/10.1038/s41419-021-04153-1.
26. Onnis B, Fer N, Rapisarda A, Perez VS, Melillo G. Autocrine production of IL-11 mediates tumorigenicity in hypoxic cancer cells. J Clin Invest. 2013;123(4):1615–29. https://doi.org/10.1172/JCI59623.
27. Liu Q, Qiao L, Liang N, Xie J, Zhang J, Deng G, Luo H, Zhang J. The relationship between vasculogenic mimicry and epithelial-mesenchymal transitions. J Cell Mol Med. 2016;20(9):1761–9. https://doi.org/10.1111/jcmm.12851.
28. Zhou Z, Yang Y, Wang F, Kleinerman ES. Neuronal repressor REST controls ewing sarcoma growth and metastasis by affecting vascular pericyte coverage and vessel perfusion. Cancers. 2020;12(6):1405. https://doi.org/10.3390/cancers12061405
29. Manzat Saplacan RM, Balacescu L, Gherman C, Chira RI, Craiu A, Mircea PA, Lisencu C, Balacescu O. The role of PDGFs and PDGFRs in Colorectal Cancer. Mediators Inflamm. 2017;2017:4708076. https://doi.org/10.1155/2017/4708076.
30. Zhang H, Bajraszewski N, Wu E, Wang H, Moseman AP, Dabora SL, Griffin JD, Kwiatkowski DJ. PDGFRs are critical for PI3K/Akt activation and negatively regulated by mTOR. J Clin Invest. 2007;117(3):730–8. https://doi.org/10.1172/jci28984.
31. Mo G, Baldwin JR, Luffer-Atlas D, Ilaria RL Jr., Conti I, Heathman M, Cronier DM. Population Pharmacokinetic modeling of Olaratumab, an Anti-PDGFRalpha Human monoclonal antibody, in patients with Advanced and/or metastatic Cancer. Clin Pharmacokinet. 2018;57(3):355–65. https://doi.org/10.1007/s40262-017-0562-0.
32. Smith CL, Baek ST, Sung CY, Tallquist MD. Epicardial-derived cell epithelial-to-mesenchymal transition and fate specification require PDGF receptor signaling. Circ Res. 2011;108(12):e15–26. https://doi.org/10.1161/CIRCRESAHA.110.235531.
33. Papadopoulos N, Lennartsson J. The PDGF/PDGFR pathway as a drug target. Mol Aspects Med. 2018;62:75–88. https://doi.org/10.1016/j.mam.2017.11.007.
34. Shang J, Gao ZY, Zhang LY, Wang CY. Over-expression of JAZF1 promotes cardiac microvascular endothelial cell proliferation and angiogenesis via activation of the akt signaling pathway in rats with myocardial ischemia-reperfusion. Cell Cycle. 2019;18(14):1619–34. https://doi.org/10.1080/15384101.2019.1629774.
35. Xia Y, Tang G, Chen Y, Wang C, Guo M, Xu T, Zhao M, Zhou Y. Tumor-targeted delivery of siRNA to silence Sox2 gene expression enhances therapeutic response in hepatocellular carcinoma. Bioact Mater. 2021;6(5):1330–40. https://doi.org/10.1016/j.bioactmat.2020.10.019.
36. Powell JE, Lim CKW, Krishnan R, McCallister TX, Saporito-Magrina C, Zeballos MA, McPheron GD, Gaj T. Targeted gene silencing in the nervous system with CRISPR-Cas13. Sci Adv. 2022;8(3):eabk2485. https://doi.org/10.1126/sciadv.abk2485.
37. Wittrup A, Lieberman J. Knocking down disease: a progress report on siRNA therapeutics. Nat Rev Genet. 2015;16(9). https://doi.org/10.1038/nrg3978. 543 – 52.
38. Wang C, Liu Q, Zhang Z, Wang Y, Zheng Y, Hao J, Zhao X, Liu Y, Shi L. Tumor targeted delivery of siRNA by a nano-scale quaternary polyplex for cancer treatment. Chem Eng J. 2021;425:130590. https://doi.org/10.1016/j.cej.2021.130590.
39. Shapiro G, Wong AW, Bez M, Yang F, Tam S, Even L, Sheyn D, Ben-David S, Tawackoli W, Pelled G, Ferrara KW, Gazit D. Multiparameter evaluation of in vivo gene delivery using ultrasound-guided, microbubble-enhanced sonoporation. J Control Release. 2016;223:157–64. https://doi.org/10.1016/j.jconrel.2015.12.001.
40. Yang J, Li Y, Jin S, Xu J, Wang PC, Liang XJ, Zhang X. Engineered biomaterials for development of nucleic acid vaccines. Biomater Res. 2015;19:5. https://doi.org/10.1186/s40824-014-0025-8.
41. Ginn SL, Amaya AK, Alexander IE, Edelstein M, Abedi MR. Gene therapy clinical trials worldwide to 2017: an update. J Gene Med. 2018;20(5):e3015. https://doi.org/10.1002/jgm.3015.
42. Finer M, Glorioso J. A brief account of viral vectors and their promise for gene therapy. Gene Ther. 2017;24(1):1–2. https://doi.org/10.1038/gt.2016.71.
43. Sung YK, Kim SW. Recent advances in the development of gene delivery systems. Biomater Res. 2019;23:8. https://doi.org/10.1186/s40824-019-0156-z.
44. Kotterman MA, Chalberg TW, Schaffer DV. Viral vectors for Gene Therapy: translational and clinical Outlook. Annu Rev Biomed Eng. 2015;17:63–89. https://doi.org/10.1146/annurev-bioeng-071813-104938.
45. Chen W, Chen H, Zheng D, Zhang H, Deng L, Cui W, Zhang Y, Santos HA, Shen H. Gene-Hydrogel Microenvironment regulates Extracellular Matrix Metabolism Balance in Nucleus Pulposus. Adv Sci (Weinh). 2020;7(1):1902099. https://doi.org/10.1002/advs.201902099.
46. Malloggi C, Pezzoli D, Magagnin L, De Nardo L, Mantovani D, Tallarita E, Candiani G. Comparative evaluation and optimization of off-the-shelf cationic polymers for gene delivery purposes. Polym Chem. 2015;6(35):6325–39. https://doi.org/10.1039/c5py00915d.
47. Wang J, Wang H, Zhao P, Chen Z, Lin Q. Hyperbranched-star PEI-g-PEG as a nonviral vector with efficient uptake and hypotoxicity for retinoblastoma gene therapy application. Colloid Interface Sci Commun. 2022;50:100647. https://doi.org/10.1016/j.colcom.2022.100647.
48. Smith N, Bade AN, Soni D, Gautam N, Alnouti Y, Herskovitz J, Ibrahim IM, Wojtkiewicz MS, Dyavar Shetty BL, McMillan J, Gendelman HE, Edagwa B. A long acting nanoformulated lamivudine ProTide. Biomaterials. 2019;223:119476. https://doi.org/10.1016/j.biomaterials.2019.119476.
49. Nam HY, McGinn A, Kim PH, Kim SW, Bull DA. Primary cardiomyocyte-targeted bioreducible polymer for efficient gene delivery to the myocardium. Biomaterials. 2010;31(31):8081–7. https://doi.org/10.1016/j.biomaterials.2010.07.025.
50. Tu T, Zhang C, Yan H, Luo Y, Kong R, Wen P, Ye Z, Chen J, Feng J, Liu F, Wu JY, Yan X. CD146 acts as a novel receptor for netrin-1 in promoting angiogenesis and vascular development. Cell Res. 2015;25(3):275–87. https://doi.org/10.1038/cr.2015.15.
51. Chen M, Qiu T, Wu J, Yang Y, Wright GD, Wu M, Ge R. Extracellular anti-angiogenic proteins augment an endosomal protein trafficking pathway to reach mitochondria and execute apoptosis in HUVECs. Cell Death Differ. 2018;25(11):1905–20. https://doi.org/10.1038/s41418-018-0092-9.
52. Cho JH, Kim MJ, Kim KJ, Kim JR. POZ/BTB and AT-hook-containing zinc finger protein 1 (PATZ1) inhibits endothelial cell senescence through a p53 dependent pathway. Cell Death Differ. 2012;19(4):703–12. https://doi.org/10.1038/cdd.2011.142.
53. Yang Y, Zhu X, Jia X, Hou W, Zhou G, Ma Z, Yu B, Pi Y, Zhang X, Wang J, Wang G. Phosphorylation of Msx1 promotes cell proliferation through the Fgf9/18-MAPK signaling pathway during embryonic limb development. Nucleic Acids Res. 2020;48(20):11452–67. https://doi.org/10.1093/nar/gkaa905.
54. Zhu S, Huang H, Liu D, Wen S, Shen L, Lin Q. Augmented cellular uptake and homologous targeting of exosome-based drug loaded IOL for posterior capsular opacification prevention and biosafety improvement. Bioact Mater. 2022;15:469–81. https://doi.org/10.1016/j.bioactmat.2022.02.019.
55. Han CY, Tang C, Guevara ME, Wei H, Wietecha T, Shao B, Subramanian S, Omer M, Wang S, O'Brien KD, Marcovina SM, Wight TN, Vaisar T, de Beer MC, de Beer FC, Osborne WR, Elkon KB, Chait A. Serum amyloid a impairs the antiinflammatory properties of HDL. J Clin Invest. 2016;126(1). https://doi.org/10.1172/JCI83475. 266 – 81.
56. Wang Y, Newman MR, Ackun-Farmmer M, Baranello MP, Sheu TJ, Puzas JE, Benoit DSW. Fracture-targeted delivery of beta-catenin agonists via peptide-functionalized nanoparticles augments Fracture Healing. ACS Nano. 2017;11(9):9445–58. https://doi.org/10.1021/acsnano.7b05103.
57. Zhang J, He M, Nie C, He M, Pan Q, Liu C, Hu Y, Chen T, Chu X. Biomineralized metal-organic framework nanoparticles enable a primer exchange reaction-based DNA machine to work in living cells for imaging and gene therapy. Chem Sci. 2020;11(27):7092–101. https://doi.org/10.1039/d0sc00339e.
58. Xu XL, Singh HP, Wang L, Qi DL, Poulos BK, Abramson DH, Jhanwar SC, Cobrinik D. Rb suppresses human cone-precursor-derived retinoblastoma tumours. Nature. 2014;514(7522):385–8. https://doi.org/10.1038/nature13813.
59. Thorne CA, Chen IW, Sanman LE, Cobb MH, Wu LF, Altschuler SJ. Enteroid Monolayers reveal an Autonomous WNT and BMP Circuit Controlling Intestinal Epithelial Growth and Organization. Dev Cell. 2018;44(5):624–e6334. https://doi.org/10.1016/j.devcel.2018.01.024.

60. Jokerst JV, Lobovkina T, Zare RN, Gambhir SS. Nanoparticle PEGylation for imaging and therapy. Nanomed (Lond). 2011;6(4):715–28. https://doi.org/10.2217/nnm.11.19.
61. Merkel OM. Can pulmonary RNA delivery improve our pandemic preparedness? J Controlled Release. 2022;345:549–56. https://doi.org/10.1016/j.jconrel.2022.03.039.
62. Wang AZ, Langer R, Farokhzad OC. Nanoparticle delivery of cancer drugs. Annu Rev Med. 2012;63. https://doi.org/10.1146/annurev-med-040210-162544. 185 – 98.
63. Hakeem A, Zahid F, Zhan G, Yi P, Yang H, Gan L, Yang X. Polyaspartic acid-anchored mesoporous silica nanoparticles for pH-responsive doxorubicin release. Int J Nanomed Volume. 2018;13:1029–40. https://doi.org/10.2147/ijn.S146955.
64. Fan B, Kang L, Chen L, Sun P, Jin M, Wang Q, Bae YH, Huang W, Gao Z. S Theranostics. 2017;7(2):357–76. https://doi.org/10.7150/thno.16855.
65. Wu J, Huang J, Kuang S, Chen J, Li X, Chen B, Wang J, Cheng D, Shuai X. Synergistic MicroRNA therapy in liver fibrotic rat using MRI-Visible nanocarrier targeting hepatic stellate cells. Adv Sci. 2019;6(5). https://doi.org/10.1002/advs.201801809.
66. Natarajan S, Foreman KM, Soriano MI, Rossen NS, Shehade H, Fregoso DR, Eggold JT, Krishnan V, Dorigo O, Krieg AJ, Heilshorn SC, Sinha S, Fuh KC, Rankin EB. Collagen Remodeling in the hypoxic tumor-mesothelial niche promotes ovarian Cancer Metastasis. Cancer Res. 2019;79(9):2271–84. https://doi.org/10.1158/0008-5472.Can-18-2616.
67. Su M, Xu X, Wei W, Gao S, Wang X, Chen C, Zhang Y. Involvement of human chorionic gonadotropin in regulating vasculogenic mimicry and hypoxia-inducible factor-1α expression in ovarian cancer cells. Cancer Cell Int. 2016;16(1). https://doi.org/10.1186/s12935-016-0327-0.
68. Chen G, Nakamura I, Dhanasekaran R, Iguchi E, Tolosa EJ, Romecin PA, Vera RE, Almada LL, Miamen AG, Chaiteerakij R, Zhou M, Asiedu MK, Moser CD, Han S, Hu C, Banini BA, Oseini AM, Chen Y, Fang Y, Yang D, Shaleh HM, Wang S, Wu D, Song T, Lee J-S, Thorgeirsson SS, Chevet E, Shah VH, Fernandez-Zapico ME, Roberts LR. Transcriptional Induction of Periostin by a sulfatase 2–TGFβ1–SMAD signaling Axis mediates Tumor Angiogenesis in Hepatocellular Carcinoma. Cancer Res. 2017;77(3):632–45. https://doi.org/10.1158/0008-5472.Can-15-2556.
69. Luo D, Wang Y, Zhang M, Li H, Zhao D, Li H, Chen X, Jin C, Han B. SOCS5 knockdown suppresses metastasis of hepatocellular carcinoma by ameliorating HIF-1alpha-dependent mitochondrial damage. Cell Death Dis. 2022;13(11):918. https://doi.org/10.1038/s41419-022-05361-z.
70. Na T-Y, Schecterson L, Mendonsa AM, Gumbiner BM. The functional activity of E-cadherin controls tumor cell metastasis at multiple steps. Proc Natl Acad Sci. 2020;117(11):5931–7. https://doi.org/10.1073/pnas.1918167117.

Publisher's note